

Electrical and Optical Properties of ZnO:Al/p-Si Heterojunction Diodes

M.A. BOUACHERIA^a, A. DJELLOUL^{b,*}, L. BENHARRAT^b,
M. ADNANE^a AND H. BENCHERIF^c

^aMaterial Technology Department, Faculty of Physics, USTO-MB, El Mnaouar Bir El Djir, BP 1505, 31000, Oran, Algeria

^bCentre de Recherche en Technologie des Semi-Conducteurs pour l'Energétique (CRTSE), 02 Bd Frantz Fanon, BP 140, 7 Merveilles, 16000, Algiers, Algeria

^cLEREESI, HNS-RE2SD, Higher National School of Renewable Energy, Environment & Sustainable Development, Constantine road, Fesdis, 05078, Batna, Algeria

Received: 01.08.2023 & Accepted: 19.10.2023

Doi: [10.12693/APhysPolA.145.47](https://doi.org/10.12693/APhysPolA.145.47)

*e-mail: djelloulcrtse@gmail.com

The study examines the optical and electrical characteristics of n-ZnO:Al (AZO) thin films that were deposited on p-Si using the sol-gel dip-coating process, with thicknesses ranging from three to six cycles. The I - V characteristics of the diode device exhibited a high and low current under forward and reverse bias, respectively. The ideality factors were found to decrease from 2.78 to 2.13 with an increase in the number of layers from 3C to 6C. However, it was revealed that the barrier height increased from 0.72 to 0.79 eV. Similarly, the rectification ratio increased from 3196 at ± 4 V to 5253 at ± 4 V with an increase in the thickness of the emitter layer. Some diode parameters were calculated according to the thermionic and Chueng models and found to be in a range comparable to the literature. The optical study based on photoluminescence under UV excitation showed typical emission spectra of n-AZO/-Si heterostructure characterized by a high emission band around 389 nm, which is due to the recombination of excitons (e^-/h^+). The various intrinsic defects present in ZnO-doped Al thin films are attributed to the broad emission band in the visible range. The chromaticity study with color properties indicated that the correlated color temperature value of the sample 3C (1380 K) falls in the warm white light region. However, the correlated color temperature value of sample 6C (4454 K) is located in the cool white light source region, which is more suitable as an LED lighting source. It was found that by increasing the emitter layer thickness, the correlated color temperature value of the 6C sample is getting closer to 6504 K — the Commission Internationale de l'Eclairage (CIE) standard for daylight (D65). However, unlike the Duv value of the 6C sample (0.011), the one of the 3C sample (0.0032) is located within the acceptable shift range (± 0.006). Based on this study, these heterostructures might be an appealing option for manufacturing W-LEDs with n-UV/blue LED chips as the excitation source for use in displays and lighting.

topics: ZnO:Al/p-Si heterojunction, photoluminescence, CIE coordinates, CCT/Duv values

1. Introduction

For many decades, zinc oxide (ZnO) has been attracting considerable attention owing to its widespread use in various applications in science and industry, particularly in optoelectronics [1–3]. ZnO is an n-type semiconductor that differs from other transition metal oxides in a number of ways, including its high level of thermal, physical, and chemical stability, high electrical conductivity, high photosensitivity, wide direct band gap (3.37 eV) in the near UV, low cost and toxicity, as well as its abundance in nature [4–6].

Along with the aforementioned benefits, ZnO still has some drawbacks, including a lack of versatility, instability when it comes to heat edging in air or environments that are corrosive, and poor

performance when exposed to visible light. Exploring this versatility also necessitates the addition of impurities to strengthen the properties. For many years, impurities were introduced into ZnO and deposited by various techniques in order to improve its properties. One may find that various metal elements (i.e., copper (Cu), indium (In), gallium (Ga), lithium (Li), iron (Fe), tin (Sn), nickel (Ni), lead (Pb), cadmium (Cd), and aluminum (Al), etc.) have been doped into ZnO host lattice [7–13]. This doping process improved the performance of the material by altering its properties. Several methods were adopted to synthesize undoped and doped ZnO thin films. Among reported methods, one finds laser deposition [14, 15], sputtering [16], molecular beam epitaxy (MBE) [17], evaporation [18], chemical vapor deposition (CVD) [19], electrochemical

deposition [20], doctor blade technique [21], chemical bath deposition (CBD) [22, 23], chemical wet and dry (CWD) method [24], successive ionic layer adsorption and reaction (SILAR) method [25], spray pyrolysis [26–29], and sol–gel process including spin and dip-coating processes [30–33]. Due to its cheap manufacturing costs, effectiveness, simplicity, simple control of doping, broad area homogeneity, and crystalline consistency during the production of devices, the sol–gel dip-coating process is suited for thin film deposition [34, 35].

In the field of diodes, ZnO as an emitter layer continues to attract great interest due to its unique properties mentioned earlier. To increase the performance of p–n junction-based diodes, several researchers continue to make significant efforts. Urper et al. [36] made Al-doped ZnO (AZO)/p-Si heterojunction diodes via sol–gel dip-coating technique under four different annealing ambient gases (argon, air, vacuum, and nitrogen). Shah et al. [37] synthesized n-ZnO/p-Si and n-AZO/p-Si heterojunctions via the spray pyrolysis method. Both used the current–voltage (I – V) measurement to confirm the rectifying diode behavior at various temperatures and light intensities. The ideality factors n for ZnO and AZO/p-Si heterojunctions have been calculated for low forward voltage, which suggests outstanding diode characteristics. Direct-current magnetron sputtering was used by Bo et al. [38] to produce n-AZO/p-Si heterojunctions on p-type single-crystal Si wafers. Current–voltage (I – V) characteristics were used to examine and thoroughly investigate the rectifying and photoelectric behavior. In this study, n-AZO/p-Si heterojunction was fabricated by depositing AZO thin films on a p-Si substrate utilizing the straightforward and affordable sol–gel dip-coating method. The I – V characteristics of the n-AZO/p-Si heterojunction were investigated as a function of emitter layer thickness both in the dark and under light. The optical properties of the obtained heterostructure were thoroughly examined using room-temperature photoluminescence (RTPL) and CIE coordinates. The color properties were investigated for possible applications in display and lighting.

2. Synthesis of the AZO/p-Si heterojunction

The deposition of AZO thin films on p-type Si (100) substrates (with a thickness of 350 nm and 1–20 Ω cm resistivity) using the sol–gel dip-coating process (Dip Coating Unit with Hot Chamber, Model No. HO-TH-02) resulted in the formation of an n-AZO/p-Si heterojunction (Fig. 1).

First, zinc acetate dehydrate (ZAD) $\text{Zn}(\text{CH}_3\text{COO})_2 \cdot 2\text{H}_2\text{O}$ was dissolved in ethanol ($\text{C}_2\text{H}_6\text{O}$) until a concentration of 0.2 M was reached. Next, monoethanolamine (MEA) $\text{C}_2\text{H}_7\text{NO}$ was added to the mixed solution as a sol stabilizer. This step was followed by the addition of the

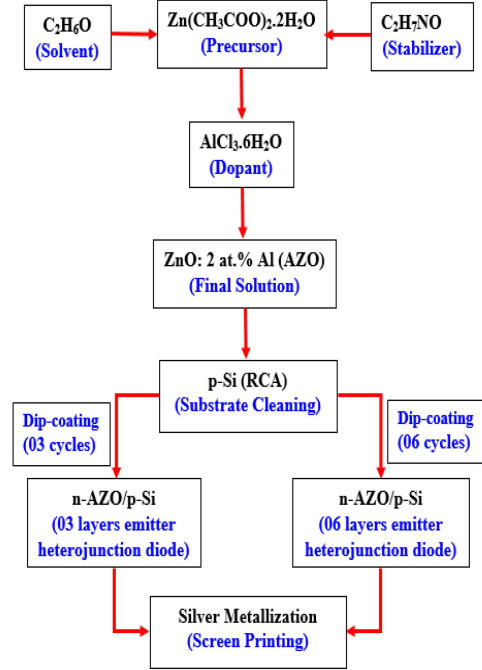


Fig. 1. A schematic view of the fabrication process of n-AZO/p-Si heterojunction.

doping agent from aluminum chloride hexahydrate ($\text{AlCl}_3 \cdot 6\text{H}_2\text{O}$), keeping the Al/Zn atomic ratio at 2%. The temperature of the final solution was maintained under stirring for 2 h at 60°C until a light yellowish homogeneous and clear solution was obtained.

To achieve two distinct thicknesses (AZO3 and AZO6) on Si substrates, two distinct coating cycles (3 and 6) were used in the dip-coating process. P-type Si (boron-doped) substrates were first cleaned with RCA (Radio Corporation of America cleaning technique) to get rid of the organic waste and metal ions before beginning the deposition process. Ag eutectic contacts (ohmic contact) were deposited as back and front contacts on the p-Si and n-AZO surfaces, respectively, for current–voltage (I – V) measurements. The devices’ active area is about $1 \times 1 \text{ cm}^2$. The schematic illustration of the AZO/p-Si heterojunction structure is depicted in Fig. 2.

3. Results and discussion

3.1. Electrical properties

The manufactured nanostructure AZO/p-Si heterojunction of diodes underwent electrical characterizations at room temperature in the absence of light. The experimental semilog I – V characteristics of rectification-capable AZO/p-Si heterojunction diodes are depicted in Fig. 1. Anderson rule is used to obtain the energy band diagram of the diode at equilibrium, which results in a large band discontinuity in the valence band offset (EV) and

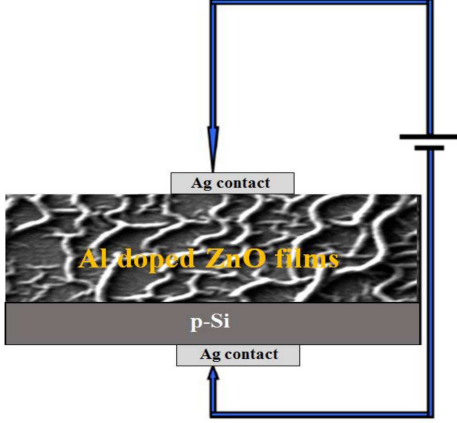


Fig. 2. The schematic structure of the n-AZO/p-Si heterojunction.

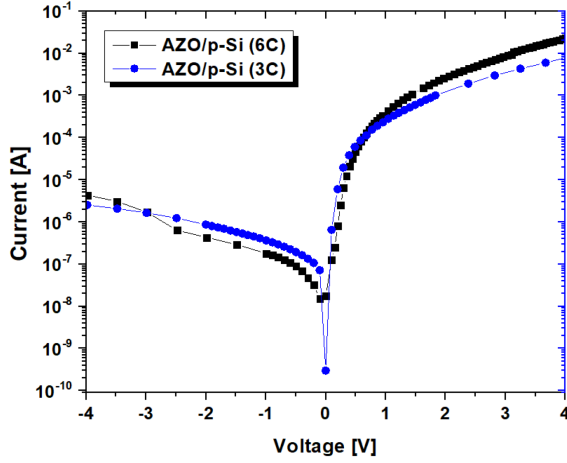


Fig. 3. Forward and reverse semilog plot of current-voltage characteristics under dark conditions of n-AZO/p-Si (3C) and n-AZO/p-Si (6C) heterojunctions.

a minor band discontinuity in the conduction band offset (EC). A significant current (majority carrier's injection) is predicted from the AZO/p-Si junction under forward bias, while an extremely low current (minority carrier's injection) is predicted from the junction under reverse bias [39].

Figure 3 demonstrates that the rectification ratio (RR), i.e., $I(+5\text{ V})/I(-5\text{ V})$, of the AZO/p-Si diode is determined to be 46090.65 based on the observed current versus bias voltage.

The relationship between current (I) and voltage (V) characteristics may be utilized to derive the diode parameters using the Shockley equation

$$I = I_s \exp\left(\frac{qV}{n k_B T} - 1\right), \quad (1)$$

which is based on the thermionic emission model [40, 41]. In (1), q and V denote the charge of the electron and the applied bias voltage, respectively; n refers to the junction ideality factor, k_B is

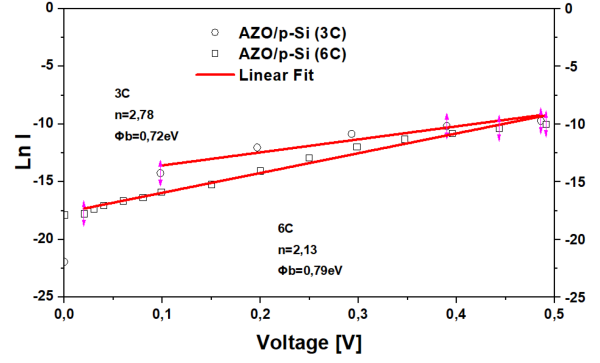


Fig. 4. Semilog scale of forward I - V plotting of n-AZO/p-Si (3C) and n-AZO/p-Si (6C) heterojunctions under dark.

Boltzmann's constant, and T is the absolute temperature. The reverse saturation current is symbolized by I_s [40] and defined as

$$I_s = A A^* T \exp\left(-\frac{q \Phi_b}{k_B T}\right), \quad (2)$$

where A is the rectifier contact area, A^* is the theoretical Richardson constant ($32\text{ A cm}^2/\text{K}^2$ for ZnO), and Φ_b is the readily determined barrier height at zero-bias in (2). The slope of the linear area of the forward bias $\ln(I)$ - V plot can be used to compute the ideality factor n , which can be expressed as [40]

$$n = \frac{q}{k_B T} \ln\left(\frac{I_s}{A A^* T^2}\right). \quad (3)$$

Additionally, (3) may be expressed as follows, if it is rearranged in accordance with the barrier height [40],

$$\Phi_b = \frac{k_B T}{q} \frac{dV}{d(\ln(I))}. \quad (4)$$

For the slight forward current area, the forward bias diode current will be roughly equivalent to the reverse saturation current. Therefore, for an applied forward voltage ($V > \frac{3k_B T}{q}$), (1) turns into [40]

$$\ln(I) = \frac{qV}{n k_B T} + \ln(I_s). \quad (5)$$

The ideality factors (n) derived from the slopes of the linear areas (Fig. 4) are equal to 2.13 and 2.78 for the samples n-AZO/p-Si (6C) and (3C), respectively. The intercept of the straight line of the $\ln(I)$ - V plot at zero-bias is used to determine the reverse saturation current (I_s), which is equal to 2.13 and 2.78 for the two samples. Both values of n are larger than unity. In general, series resistances and the existence of interface states are held responsible for high values of n .

With the use of (4), we calculated the barrier heights (Φ_b). The obtained values were 0.79 eV and 0.72 eV for 6C and 3C, respectively. The computed values in this study are within reasonable limits, considering that the difference between the semiconductor electron affinities of Si ($= 4.97\text{ eV}$) and

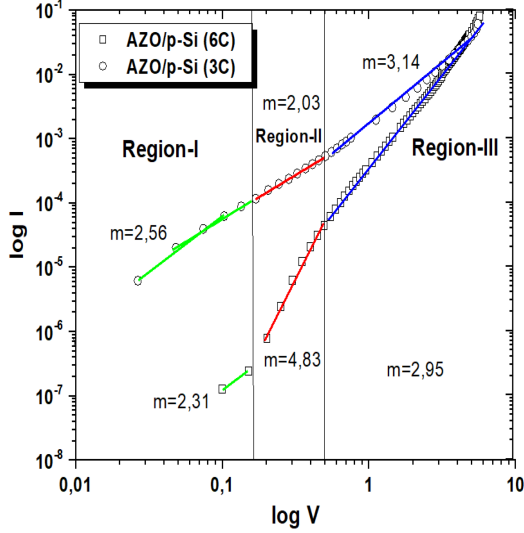


Fig. 5. The $\log(I)$ vs $\log(V)$ characteristics of the heterojunction.

ZnO ($= 4.25$ eV) is 0.72 eV. When the n , I_s , and Φ_b values are evaluated with respect to those reported in the literature [42–47], we see that the value of Φ_b tends to rise as the AZO layer's thickness rises. This variation in Φ_b is elucidated by the image force resulting from the image width depletion region. AZO (6C) has a lower I_s , a higher Φ_b , and a relatively lesser n value compared to those in the literature [42–47]. It is worth mentioning that high Φ_b values would be desirable in order to reduce I_s and improve the rectification ratio (RR). Thereby, RR increases with the increasing thickness of the AZO layer. In order to better comprehend the charge transport mechanism in the Si/ZnO heterojunction, the logarithmic graph of current–voltage ($\log(I)$ – $\log(V)$) under forward bias has been investigated. According to Fig. 5, there are three zones on the plot, indicating different conduction mechanisms. (i) Region-I is the low forward voltage area (0.05 – 0.2 V), and the computed slopes (m) for 6C and 3C, respectively, are 2.19 and 2.34 . This shows that the space-charge-limited current (SCLC) mechanism governs the conduction mechanism of the n-AZO/p-Si heterojunction in this voltage range [48, 49]. (ii) In Region-II (0.4 – 1 V), only AZO/p-Si (6C) fluctuates exponentially with voltage, and the slope of $m = 4.83$ is observed, indicating that the trapped-charge-limited current (TCLC) is responsible for the current [50–53]. In this mechanism, the energy distribution of trap levels within the forbidden band causes the slope to be greater than 2. (iii) Region-III is the high junction voltage area (1 – 4 V), which has an exponential distribution of trapping levels because the slope $m > 3$. This finding is in good accord with the results from the reference study [54]. This study revealed that the current–voltage characteristics follow a power law ($I \sim VL$) in Region III.

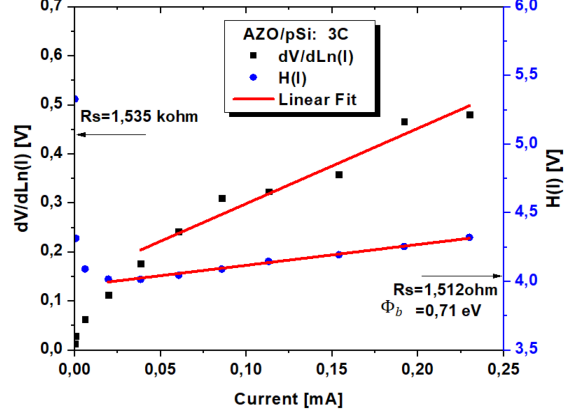


Fig. 6. Plots of $dV/d\ln(I)$ and $H(I)$ as a function of current (I) of AZO/p-Si (3C) device in the dark.

Series resistance (R_s) and interface states/traps or dislocations cause the I – V characteristics of the devices to deviate from linearity at high forward voltages. The following equation represents the I – V characteristics in terms of the thermionic emission (TE) model

$$I = I_s \exp\left(\frac{q(V - R_s I)}{n k_B T} - 1\right), \quad (6)$$

where $R_s I$ represents the voltage drop across the heterojunction diode series resistance, which is important and influences how the device behaves. The technique suggested by Cheung et al. [55] and represented by the ensuing equation was used to obtain the series resistance

$$\frac{dV}{d(\ln(I))} = R_s I + \frac{n k_B T}{q}. \quad (7)$$

Figures 6 and 7 represent the plots of $dV/d(\ln(I))$ versus I for the samples (3C) and (6C), respectively. The intercepts of the slope and the y -axis are used to calculate R_s . These values are listed in Table I [52, 54, 56–64]. The following Cheung's equations [55] provide the function H as a function of current (I), which may be plotted to determine Φ_b and R_s

$$H(I) = V - \frac{n k_B T}{q} \ln\left(\frac{I}{A A^* T^2}\right) = R_s I + n \Phi_b. \quad (8)$$

The plots of H function with respect to current I are shown in Figs. 6 and 7 for the samples (3C) and (6C), respectively. It is observed that $H(I)$ rises linearly as current I rises. The slope of the curve is employed to calculate the value of R_s . Using the ideality factor determined by (7), the barrier height Φ_b is computed from the y -intercept. All results for the devices are displayed in Table I. The R_s values calculated from the dependence $H(I)$ are close to the values obtained by the thermionic emission model.

To clarify the barrier heterogeneity found in conventional TE theory, several researchers [65–67] examined a system of discrete interface areas of Φ_b .

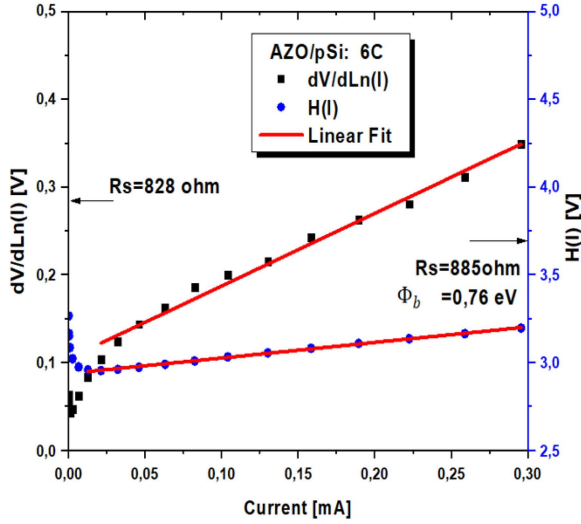
Extracted AZO/p-Si heterojunction parameters and literature comparison.

TABLE I

n	I_s [A]	Φ_b [eV]	RR	R_s [k Ω] = $dV/d\ln(I)$	R_s [k Ω] H function	Φ_b [eV]	Deposit technique (AZO layer)	Ref.
2.78	2.52×10^{-7}	0.78	3196@ ± 4 V	1.535	1.512	0.71	sol-gel (3 cycles)	our work
2.13	1.93×10^{-8}	0.85	5253@ ± 4 V	0.828	0.885	0.76	sol-gel (6 cycles)	our work
2.70	6.00×10^{-8}	0.70	52@ ± 5 V	0.750	0.730	0.70	chem. bath dep.	[56]
5.90	1.10×10^{-7}	0.78	923@ ± 4 V	0.243	0.118	0.79	sol-gel	[57]
1.43	1.24×10^{-9}	0.825	25867@ ± 5 V	–	–	–	APCVD*	[58]
1.96	–	0.70	–	5.070	10.340	0.49	chem. bath dep.	[52]
10	1.00×10^{-6}	0.696	22@ ± 3 V	3.2	–	–	chem. bath dep.	[59]
2.16	3.66×10^{-8}	0.59	7530@ ± 2 V	76	88	0.63	RF sputtering	[60]
2.66	–	0.80	–	301	–	0.98	chem. bath dep.	[54]
2.38	1.10×10^{-7}	0.74	40@ ± 4 V	2.69	2.706	0.85	chem. bath dep.	[61]
2.20	1.26×10^{-10}	0.79	995@ ± 5 V	75	75.4	0.72	sol-gel	[62]
3.20	–	0.74	840@ ± 5 V	–	–	–	RF sputtering	[63]
–	7.33×10^{-9}	0.87	–	6.280	5.6	0.90	spray pyrolysis	[64]

*

atmospheric pressure CVD


 Fig. 7. Plots of $dV/d\ln(I)$ and $H(I)$ as a function of current (I) of AZO/p-Si (6C) device in the dark.

Even at scales far lower than the width of the depletion area (WD), the change in Φ_b may still occur. Because of this, it is likely that the presence of barrier inhomogeneities at the interface will significantly affect the charge transport mechanism across the diodes. Additionally, it should be remembered that the ideality factor, which determines the degree of lateral Φ_b inhomogeneity at the actual diode interfaces, rises with lowering zero-bias Φ_b [68].

The extracted parameters of the AZO/p-Si heterojunction were compared with the results reported in the literature, as exposed in Table I. The values of R_s for our heterojunction are smaller than the values reported by [54, 56–59, 64] and higher for

the others. However, barrier heights (Φ_b) and ideality factors (n) are in agreement with the reported values.

The electrical parameters extracted for n-AZO/p-Si heterojunction have been compared with the literature, as shown in Table I. The ideality factors n were found to decrease from 2.78 to 2.13 with an increasing number of layers from 3C to 6C, which is in the same order of magnitude as the findings reported in [54, 56, 60–62]. In the same direction, the saturation current (I_s) was found to decrease under doubling thickness while remaining closer to values given in the literature [57, 60, 61, 66]. However, the barrier height increased for both models, remaining close to the compared references. Similarly, the rectification ratio increased from 3196 at ± 4 V to 5253 at ± 4 V with increasing thickness of the emitter layer, showing a large discrepancy with the reference values. The values of series resistances decreased from 1.535 and 1.512 k Ω to 0.828 and 0.885 k Ω , as obtained from $dV/d\ln(I)$ and H function by doubling the number of cycles, respectively. These values are comparable to those found in [56, 57], however lower than the values reported by [52, 60–62, 64].

Figure 8 displays the I – V characteristics of the AZO/p-Si heterojunction diode in both dark and light conditions. Optical radiation causes an augment in the forward and reverse currents. The rise in reverse current is far higher than anticipated. This shows that the I – V curve of the AZO/p-Si heterojunction is altered by the amount of photocurrent, indicating that it is a photodiode. The structure's depletion zone, where light induces electron generation, is where the photoelectric effect occurs [69].

3.2. Photoluminescence study

Photoluminescence (PL) indeed stands out as a potent spectroscopic technique for delving into the luminescent characteristics of materials and unraveling the mechanisms governing their emissions. In line with this, Fig. 9 presents the room-temperature PL spectra associated with the heterostructure formed by the samples (3C and 6C), both synthesized with a consistent Al doping concentration of 2 wt%. The spectra were acquired within an energy range from 3.8 to 1.2 eV (325–1000 nm) using a UV excitation source with an energy of 3.82 eV (325 nm). Overall, well-crystallized ZnO exhibits a distinct and intense UV emission, primarily attributed to the recombination of free excitons consisting of electron–hole pairs (denoted as e^-/h^+) [70]. This process is often referred to as near-band-edge emission (NBE). Additionally, ZnO displays a broad and less intense visible emission, which arises from deep-level defects. Notably, both of our samples exhibit these characteristic behaviors. However, a slight alteration in the shape of the PL spectra can be discerned. This change is ascribed to variations in the contribution of defects in the de-excitation process.

In accordance with multiple reports [71–74], the most frequently observed mid-gap electronic states in ZnO are linked to various factors. These include the free exciton (FX, situated 0.06 eV from the conduction band minimum or CBM) and intrinsic defects such as zinc interstitials (Zn_i , positioned 0.22 eV below CBM), zinc vacancies (V_{Zn} , located 0.30 eV above the valence band maximum or VBM), oxygen interstitials (O_i , found 1.09 eV above VBM), and oxygen vacancies (V_O , with energy levels at 1.65 eV and 0.9 eV below CBM). Besides, extended states associated with zinc interstitials ($ex-Zn_i$) have been reported to reside within the energy range from 0.54 to 0.635 eV below CBM in ZnO [75]. As demonstrated in Fig. 9,

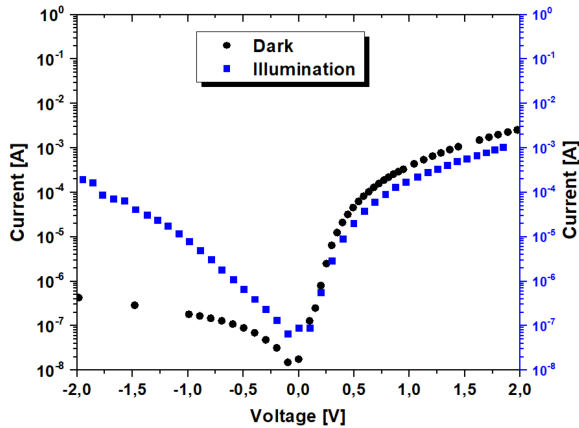


Fig. 8. Current–voltage characteristics curves AZO/p-Si heterojunction under dark and illumination.

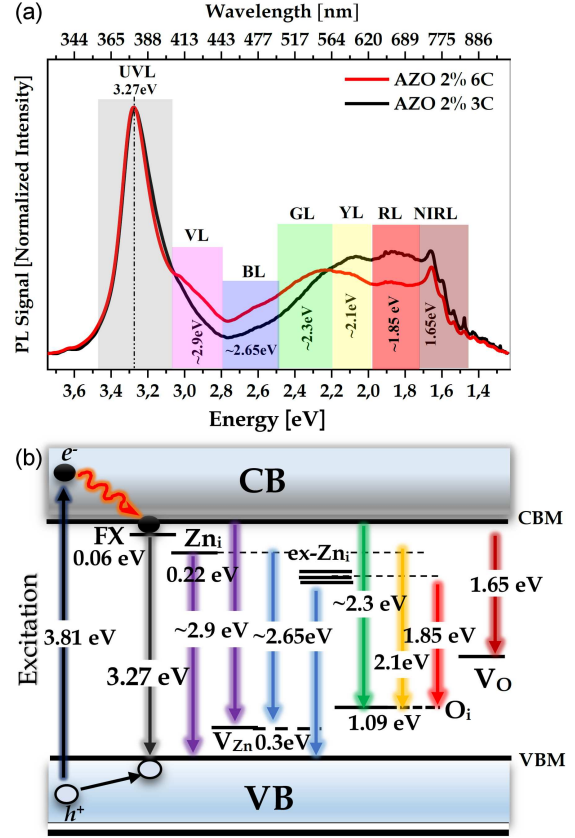


Fig. 9. (a) Room-temperature PL spectra of AZO thin films deposited on p-type Si substrates under an excitation wavelength of 325 nm. (b) Energy level diagram showing the mechanism of main defect emissions.

PL emission from ZnO can be categorized into two distinct bands within the UV region. These are referred to as UV luminescence (UVL) with an energy of 3.27 eV and violet luminescence (VL) centered at approximately 2.9 eV. Additionally, the visible region of the spectrum reveals five discernible components: blue luminescence (BL) centered around 2.65 eV, green luminescence (GL) at roughly 2.3 eV, yellow luminescence (YL) at 2.1 eV, red luminescence (RL) at 1.85 eV, and near-infrared luminescence (NIRL) at 1.65 eV. As mentioned above, UVL is due to NBE emission and originated from FX recombination. Whereas, the possible electronic transitions responsible for VL are $Zn_i \rightarrow VBM$ and/or $CBM \rightarrow V_{Zn}$ transitions [71, 73]. BL, GL, YL, and RL bands can be generated from $Zn_i \rightarrow V_{Zn}/ex-Zn_i \rightarrow VBM$, $CBM \rightarrow O_i$, $Zn_i \rightarrow O_i$, and $ex-Zn_i \rightarrow O_i$ transitions. Finally, NIRL at 1.65 eV has been attributed to $CBM \rightarrow V_O$ electronic transition [74]. All these mechanisms are summarized in the energy level diagram shown in Fig. 9b.

Comparing the two samples, it becomes evident that as the cycle number increases (6C), there is a notable enhancement in the VL and BL bands, accompanied by a reduction in the YL and RL ones. This observation suggests an increase in the Zn_i

TABLE II

CIE coordinates and CCT/Duv calculated for ZnO:2% Al thin films.

Samples	CIE 1931		CCT [K]	Duv	CIE 1976	
	x	y			u'	v'
3C	0.427	0.409	1380	0.0032	0.243	0.524
6C	0.367	0.392	4454	0.0112	0.211	0.505

and ex-Zn_i defect levels, which in turn leads to a higher rate of recombination of electrons involved in Zn_i → VBM and ex-Zn_i → VBM transitions. Consequently, this results in a decrease in their contribution to deep-level defects (Zn_i → O_i and ex-Zn_i → O_i).

As a result, the presence of the Zn_i defect, acting as a shallow donor, likely contributes to the improvement in electrical properties. Specifically, Zn_i introduces additional electrons into the conduction band. These extra electrons are positioned relatively close to CBM and demand minimal energy to become mobile charge carriers. Consequently, the introduction of Zn_i defects augments the concentration of free electrons within the ZnO material, thus resulting in enhanced electrical conductivity.

3.3. CIE coordinates, CCT/Duv and color properties

The determination of chromatic coordinates according to *Commission Internationale de l'Éclairage (CIE)*, known in English as the International Commission on Illumination, and correlated color temperature (CCT) of ZnO:2% Al thin films were performed from emission spectra under $\lambda_{ex} = 325$ nm (Table II). CIE coordinates and CCT are interesting parameters in defining if the samples with a specific emission intensity can be useful for display or lighting applications. CCT is a measurement of how yellow or blue the light emitted by a light bulb appears. It is measured in Kelvin degrees and is most commonly found between 2200 and 6500 K. CIE coordinates were calculated according to CIE 1931 and CIE 1976 colorimetry standards (Table II) and are represented in Fig. 10a and b, respectively. The additional metric, Duv (short for “Delta u,v”), measures the distance between the test light source’s coordinate of chromaticity and the nearest spot on the Planckian locus (Fig. 10a). It is typically used in conjunction with a CCT value to describe how close is a specific light source to the black body curve (pure white). When discussing color-sensitive lighting applications, Duv is an important metric to consider. This is because the CCT alone does not reveal sufficient details about the precise color. The procedure of parameter calculation in Table II can be found in detail elsewhere [76].

Lamps with a CCT 3200 K are often thought of as “warm” sources (yellowish-white through red),

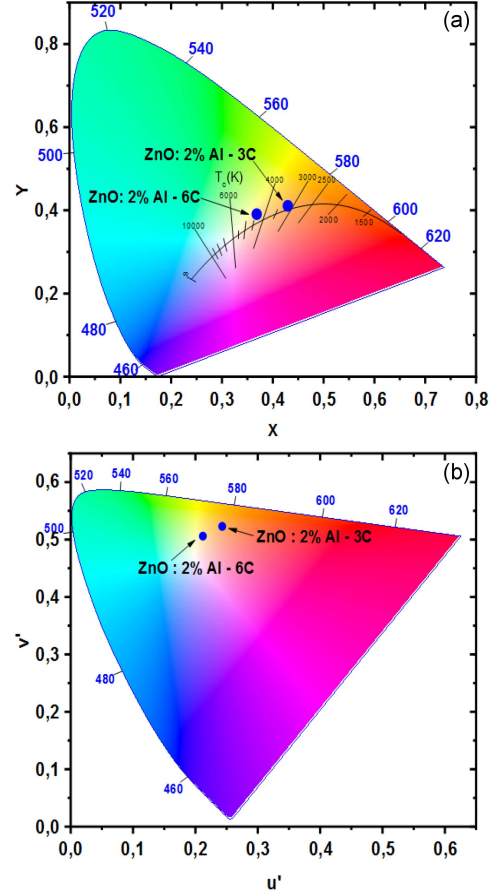


Fig. 10. Chromatic coordinates of ZnO:2% Al thin films according to (a) CIE 1931 and (b) CIE 1976 standards.

whilst those with a CCT > 4000 K are thought of as “cool” sources (bluish-white) [77]. According to Fig. 9a, the CCT value of the sample 3C (1380 K) falls in the warm white light region (CCT < 3200 K) above the tungsten lamp (2836 K) [78], which is closer to 200 W or higher light bulb for movie cameras and flash bulbs. However, the CCT value of the sample 6C (4454 K) is located in the cool white light source region (CCT > 4000 K) above those of the fluorescent tube (3937 K) [78], which is equivalent to daylight observed 2 h after sunrise, showing its more appropriateness to employ as a LED source in homes, hospitals, and office spaces, etc.

It has also been observed that with increasing the emitter layer thickness from 3C to 6C, CCT of the latter gets closer to 6504 K, which is CCT of D-65 illuminate, the CIE standard for daylight [79]. The CIE coordinates of the 6C sample are (0.367, 0.392), which is near the standard equal energy point value (0.333, 0.333), representing white light emission. Furthermore, both Duv values of the samples are positive (Table II), which indicates the blue points above the black body curve. However, unlike the Duv of the 6C sample (0.011), the one of the 3C sample (0.0032) is located within the acceptable

shift range (± 0.006) for many organizations, such as the US National Institute of Standards and Technology (ANSI) and Energy Star [80–82].

4. Conclusions

In this work, the optical and electrical properties of n-AZO/p-Si heterojunctions were investigated. AZO thin films were deposited onto p-Si substrates via a simple and low-cost sol-gel dip-coating technique with 3 and 6 cycles. The manufactured n-AZO/p-Si heterojunction device's I - V characteristics showed that the current was strong under forward bias and very low under reverse bias. The ideality factors (n) dropped from 2.78 and 2.13 for the samples of n-AZO/p-Si (3C) and (6C), respectively, as the number of layers increased. However, the barrier height (Φ_b) was found to increase with doubling the number of layers (0.72 eV and 0.79 eV for 3C and 6C, respectively). The rectification ratio (RR) increased from 3196 to 5253 at ± 4 V with increasing thickness of the emitter layer. Some diode parameters were calculated according to the thermionic and Chueng models and found to be in a range comparable to the literature. The optical properties studied by PL showed typical emission spectra of AZO thin films characterized by high emission band around 389 nm, which is due to the excitons (e^-/h^+) recombination. The wide emission band in the visible region is attributed to different intrinsic defects in ZnO-doped Al thin films. A chromaticity analysis that took into account color attributes demonstrated that the investigated heterostructures could be taken into consideration as a viable option for W-LED manufacturing using an n-UV/blue LED chip as the excitation source.

Acknowledgments

The Algerian Ministry of Higher Education and Scientific Research supported this research.

References

- [1] Z.C. Feng, *Handbook of Zinc Oxide and Related Materials: Volume One, Materials*, Taylor & Francis Group, CRC Press, 2013.
- [2] A.B. Djuriscic, A.M.C. Ng, X.Y. Chen, *Prog. Quant. Electron.* **34**, 191 (2010).
- [3] A.G. Martinez, G. Santana, F. Güell, P.R. Martínez-Alanis, A. Dutt, *Nanomaterials (Basel)* **10**, 857 (2020).
- [4] G. Voicu, D. Miu, C. Ghitulica, S.I. Jinga, A.I. Nicoară, C. Busuioc, A.M. Holban, *Ceram. Int.* **46**, 3904 (2020).
- [5] I. Ji, Y. Kim, J.-Y. Leem, H. Park, S. Kim, J.S. Kim, J.S. Kim, *J. Kor. Phys. Soc.* **64**, 1581 (2014).
- [6] A. Chanda, S. Gupta, M. Vasundhara, S.R. Joshi, G.R. Mutta, J. Singh, *RSC Adv* **7**, 50527 (2017).
- [7] R. Koutavarapu, R.K.N.R. Manepalli, B.T.P. Madhav, M.C. Rao, Jaesool Shim, *J. Mater. Sci. Mater. Electron.* **32**, 11264 (2021).
- [8] L.M. Mahajan, C.K. Kasar, D.S. Patil, *Mater. Res. Express.* **6**, 045053 (2019).
- [9] A. Zaier, F. Oum El az, F. Lakfif, A. Kabir, S. Boudjadar, M.S. Aida, *Mater. Sci. Semicond. Process.* **12**, 207 (2009).
- [10] F. Yang, J. Song, X. Chen, X. Lu, J. Li, Q. Xue, B. Han, X. Meng, J. Li, Y. Wang, *Solar Energy* **228**, 168 (2021).
- [11] C. Zegadi, A. Abderrahmane, A. Djelloul, S. Hamzaoui, M. Adnane, D. Chaumont, K. Abdelkebir, *Int. Rev. Phys.* **9**, 1 (2015).
- [12] A.P. Jeyakumari, P. Siva, P. Pachamuthu, M. Revathi, *IOSR J. Appl. Phys.* **3**, 80 (2017).
- [13] N. Saxena, R. Sharma, A. Hus-sain, R.J. Choudhary, A.K. Debnath, O.P. Sinha, R. Krishna, *Mater. Lett.* **306**, 130886 (2022).
- [14] R.K. Jamal, M.A. Hameed, K.A. Adem, *Mater. Lett.* **132**, 31 (2014).
- [15] S. Venkatachalam, Y. Iida, Y. Kanno, *Superlattices Microstruct.* **44**, 127 (2008).
- [16] B. Sarma, D. Barman, B.K. Sarma, *Appl. Surf. Sci.* **479**, 786 (2019).
- [17] T. Ohgaki, N. Ohashi, H. Kakemoto, S. Wada, Y. Adachi, H. Haneda, T. Tsurumi, *J. Appl. Phys.* **93**, 1961 (2003).
- [18] H. Ahmoum, G. Li, S. Belakry, M. Boughrara, M.S. Suáit, M. Kerouad, Q. Wang, *Mater. Sci. Semicond. Process.* **123**, 105530 (2021).
- [19] M. Purica, E. Budianu, E. Rusu, M. Danila, R. Gavrilă, *Thin Solid Films* **403–404**, 485 (2002).
- [20] M. Harati, D. Love, W.M. Lau, Z. Ding, *Mater. Lett.* **89**, 339 (2012).
- [21] N. Hourri, A. Djelloul, M. Adnane, *J. Nano-Electron. Phys.* **12**, 06004 (2020).
- [22] S. Shahzad, S. Javed, M. Usman, *Front. Mater.* **8**, 613825 (2021).
- [23] A.F. Abdulrahman, S.M. Ahmed, N.M. Ahmed, M.A. Almessiere, *Crystals* **10**, 386 (2020).
- [24] S. Dasgupta, J.B. Sangri, F.A. Ali, P. Pattanaik, S.K. Kamilla, in: *Proc. of ICI-CCT 2019 – System Reliability, Quality Control, Safety, Maintenance and Management*, 2020, p. 269.

- [25] D. Krishnan, P. Sreedev, V. Rakesh, N.S. Roshima, B. Shankar, S.M. Sunil, *AIP Conf. Proc.* **2162**, 020132 (2019).
- [26] V.G. Nair, R. Jayakrishnan, J. John, J.A. Salam, A.M. Anand, A. Raj, *Mater. Chem. Phys.* **247**, 122849 (2020).
- [27] A. Djelloul, Y. Larbah, M. Adnane, B. Labdelli, M.I. Ziane, A. Manseri, A. Messaoud, *J. Nano- Electron. Phys.* **10**, 02036 (2018).
- [28] S.K. Swami, N. Chaturvedi, A. Kumar, V. Kumar, A. Garg, V. Dutta, *Solar Energy* **231**, 458 (2022).
- [29] M. Melouki, H.F. Mehnane, A. Djelloul, Y. Larbah, M. Adnane, *J. Nano- Electron. Phys.* **13**, 04004 (2021).
- [30] M. Carofiglio, S. Barui, V. Cauda, M. Laurenti, *Appl. Sci.* **10**, 5194 (2020).
- [31] M. Ayachi, F. Ayad, A. Djelloul, L. Benharrat, S. Anas, *Semiconductors* **55**, 566 (2021).
- [32] J. Wojnarowicz, T. Chudoba, W. Lojkowski, *Nanomaterials* **10**, 1086 (2020).
- [33] G. Demircan, E.F. Gurses, A. Acikgoz, S. Yalcin, B. Aktas, *Mol. Cryst. Liquid Cryst.*, **709**, 61 (2020).
- [34] M.A. Bouacheria, A. Djelloul, M. Adnane, Y. Larbah, L. Benharrat. *J. Inorg. Organomet. Polym. Mater.* **32**, 2737 (2022).
- [35] I.Y.Y. Bu, *Ceram. Int.* **39**, 8073 (2013).
- [36] O. Urper, O. Karacasu, H. Cimenoglu, N. Baydogan, *Superlattices Microstruct.* **125**, 81 (2019).
- [37] M.A.H. Shah, M.K.R. Khan, A.M.M. Tanveer Karim, M.M. Rahman, M. Kamruzzaman, *J. Electron. Mater.* **47**, 1 (2018).
- [38] H. Bo, M.Z. Quan, X. Jing, Z. Lei, Z.N. Sheng, L. Feng, S. Cheng, S. Ling, Z.C. Yue, Y.Z. Shan, Y.Y. Ting, *Mater. Sci. Semicond. Process.* **12**, 248 (2009).
- [39] L.J. Brillson, Y. Lu, *J. Appl. Phys.* **109**, 121301 (2011).
- [40] K. Ozel, A. Atilgan, N.E. Koksall, A. Yildiz, *J. Alloys Compds.* **849**, 156628 (2020).
- [41] E. Arslan, Y. Badali, M. Aalizadeh, S. Altındal, E. Özbay, *J. Phys. Chem. Solids* **148**, 1098758 (2021).
- [42] S. Sharma, C. Periasamy, *Superlattices Microstruct.* **73**, 12 (2014).
- [43] F.Z. Bedia, A. Bedia, B. Benyoucef, S. Hamzaoui, *Phys. Proc.* **55**, 61 (2014).
- [44] P. Klason, M.M. Rahman, Q.H. Hu, O. Nur, R. Turan, M. Willander, *Microelectron. J.* **40**, 706 (2009).
- [45] N. Zebbar, Y. Kheireddine, K. Mokeddem, A. Hafdallah, M. Kechouane, M.S. Aida, *Mater. Sci. Semicond. Process.* **14**, 229 (2011).
- [46] L. Shen, H.W. Du, H. Ding, J. Tang, Z.Q. Ma, *Mater. Sci. Semicond. Process.* **13**, 339 (2010).
- [47] A. Alyamani, A. Tataroğlu, L. El Mir, Ahmed A. Al-Ghamdi, H. Dahman, W.A. Farooq, F. Yakuphanoglu, *Appl. Phys. A* **122**, 297 (2016).
- [48] Ş. Aydoğan, K. Çınar, H. Asıl, C. Coşkun, A. Türüt, *J. Alloys Compd.* **476**, 913 (2009).
- [49] G.B. Sakr, S.S. Fouad, I.S. Yahia, D.M.A. Basset, F. Yakuphanoglu, *Mater. Res. Bull.* **48**, 752 (2013).
- [50] D. Sang, Q. Wang, Q. Wang, D. Zhang, H. Hu, W. Wang, B. Zhang, Q. Fan, H. Li, *RSC Adv.* **8**, 28804 (2018).
- [51] F. Gao, D. Zhang, J. Wang, H. Sun, Y. Yin, Y. Sheng, S. Yan, B. Yan, C. Sui, Y. Zheng, Y. Shi, J. Liu, *Appl. Phys. Lett.* **108**, 261103 (2016).
- [52] S. Ilican, K. Gorgun, S. Aksoy, Y. Caglar, M. Caglar, *J. Mol. Struct.* **1156**, 675 (2018).
- [53] M.A. Rafiq, *J. Semicond.* **39**, 6 (2018).
- [54] Y. Caglar, K. Gorgun, S. Ilican, M. Caglar, F. Yakuphanoglu, *Appl. Phys. A* **122**, 733 (2016).
- [55] S.K. Cheung, N.W. Cheung, *Appl. Phys. Lett.* **9**, 85 (1986).
- [56] S.M. Faraz, W. Shah, N.U.H. Alvi, O. Nur, Q.U. Wahab, *Adv. Condensed Matter Phys.* **2020**, 1 (2020).
- [57] O.F. Goktas, N.E. Koksall, O. Kaplan, A. Yildiz, *J. Mater. Sci. Mater. Electron.* **32**, 7791 (2021).
- [58] Y.H. Mohammed, *Superlattices Microstruct.* **131**, 104 (2019).
- [59] R. Labar, T.K. Kundu, *J. Electron. Mater.* **47**, 3628 (2018).
- [60] S.K. Akay, S. Sarsıcı, H.K. Kaplan, *Opt. Quant. Electron.* **50**, 362 (2018).
- [61] R.N. Gayen, S.R. Bhattacharyya, *J. Phys. D Appl. Phys.* **49**, 115102 (2016).
- [62] L. Agarwal, B.K. Singh, S. Tripathi, P. Chakrabarti, *Thin Solid Films* **612**, 259 (2016).
- [63] S. Sharma, B.C. Bayer, V. Skakalova, G. Singh, C. Periasamy, *IEEE Trans. Electron. Devices* **63**, 1949 (2016).
- [64] A. Bedia, F.Z. Bedia, B. Benyoucef, S. Hamzaoui, *Phys. Procedia* **55**, 53 (2014).
- [65] Z. Tekeli, S. Altındal, M. Çakmak, S. Özçelik, *J. Appl. Phys.* **102**, 054510 (2007).

- [66] R.T. Tung, *Phys. Rev. B* **45**, 13509 (1992).
- [67] R.T. Tung, *J. Appl. Phys.* **88**, 7368 (2000).
- [68] M. Somnath, J. Puigdollers, *Phys. B Condensed Matter* **530**, 327 (2018).
- [69] T. Ootsuka, Z. Liu, M. Osamura, Y. Fukuzawab, R. Kuroda, Y. Suzuki, N. Ootogawa, T. Mise, S. Wang, Y. Hoshino, Y. Nakayama, H. Tanoue, Y. Makita, *Thin Solid Films* **476**, 30 (2005).
- [70] K. Bandopadhyay, J. Mitra, *RSC Adv.* **5**, 23540 (2015).
- [71] S. Vempati, J. Mitra, P. Dawson. *Nanoscale Res. Lett.* **7**, 470 (2012).
- [72] A. Galdámez-Martínez, G. Santana, F. Güell, P.R. Martínez-Alanis, A. Dutt, *Nanomaterials* **10**, 857 (2020).
- [73] M. Abdelkrim, M. Guezzoul, M. Bedrounia, M. Bouslama, A. Ouerdanea, B. Kharroubic, *J. Alloys Compd.* **920**, 165703 (2022).
- [74] M. Bedrouni, B. Kharroubi, A. Ouerdane, M. Bouslama, M. Guezzoul, Y. Caudano, K.B. Bensassi, M. Bousmaha, M.A. Bezzerrouk, A. Mokadem, M. Abdelkrim, *Opt. Mater.* **111**, 110560 (2021).
- [75] F. Kayaci, S. Vempati, I. Donmez, N. Biyikli, T. Uyar, *Nanoscale* **6**, 10224 (2014).
- [76] D. Durmus, *Lighting Res. Technol.* **54**, 363 (2022).
- [77] G. Lakshminarayana, S.O. Baki, A. Lira, I.V. Kityk, U. Caldiño, K.M. Kaky, M.A. Mahdi, *J. Lumin.* **186**, 283 (2017).
- [78] E.C. Fuchs, C. Sommer, F.P. Wenzl, B. Bitschnau, A.H. Paulitsch, A. Mühlanger, K. Gatterer, *Mater. Sci. Eng. B* **156**, 73 (2009).
- [79] E.J. Crace, A.C. Su, H.I. Karunadasa, *Chem. Sci.* **13**, 9973 (2022).
- [80] Calculate Duv from CIE 1931 xy Coordinates, Accessed: 05.09.2022.
- [81] Y. Ohno, "Color Quality of Lighting and Metrics — Where are we going to?", *EPA Energy Star Lighting Webinar Series Evaluating Color Quality*, National Institute of Standards and Technology, Gaithersburg (MD) 2016.
- [82] Lighting Services Inc, Consistency of the White Light LumeLEX™ 2000 Product Family, Accessed: 05.09.2022.